SPECIAL ISSUE ARTICLE

THE CANADIAN JOURNAL OF CHEMICAL ENGINEERING

Response of shear-activated nanotherapeutic particles in a clot-obstructed blood vessel by CFD-DEM simulations

Lorenzo Vasquez Giuliano[1] | Antonio Buffo[1] | Marco Vanni[1] |
Alessandra Sabina Lanotte[2,3] | Valentina Arima[2] | Monica Bianco[2] |
Francesca Baldassarre[4] | Graziano Frungieri[1]

[1]Department of Applied Science and Technology, Politecnico di Torino, Torino, Italy

[2]CNR NANOTEC, Institute of Nanotechnology, Lecce, Italy

[3]INFN, Sez. Lecce, Lecce, Italy

[4]Dipartimento di Scienze e Tecnologie Biologiche e Ambientali, Università del Salento & UdR INSTM Salento, Lecce, Italy

Correspondence

Graziano Frungieri, Department of Applied Science and Technology, Politecnico di Torino, Corso Duca degli Abruzzi 24, Torino, 10129, Italy.
Email: graziano.frungieri@polito.it

Abstract

In recent years, targeted drug delivery systems have been regarded as a promising solution to enhance the efficiency of treatments against clots in blood vessels. In this context, shear-activated nanotherapeutics (SANTs) have been recently proposed. These are micrometric clusters of polymeric nanoparticles coated with a clot lysing agent. These drug carriers are stable under normal blood flow conditions, but they can be designed to undergo breakup right on the clot in response to the local increase in the hydrodynamic stress caused by the lumen restriction, effectively concentrating the active agent at the point of need. The aim of this work is to investigate the mechanical response of three potential drug carrier morphologies to the pathological flow field stress, typically encountered in obstructed blood vessels. Computational fluid dynamics simulations have been used to compare the viscous stress in arterial obstructions with the one in a microfluidic device, suitable for in vitro experimental tests. Discrete element method simulations built upon Stokesian dynamics were conducted to estimate the tensile stress distribution acting inside isostatic, random close packing, and hollow drug carriers. The results herein presented constitute a platform for a future experimental campaign and aim at establishing SANTs as a robust and broadly applicable targeting strategy.

KEYWORDS

CFD, discrete element method, microfluidics, targeted drug delivery, thrombosis

1 | INTRODUCTION

The obstruction with clots of critical blood vessels may lead to a variety of life-threatening ischemic conditions, and it is recognized as a worldwide leading cause of death. The only treatment approved by the Food and Drug Administration is a tissue plasminogen activator (tPA), a protein that is able to dissolve the clot, restoring normal blood flow and preventing the major consequences that can be led to by ischemic events.[1,2] However, this treatment requires a prompt administration of the active agent and a careful choice of the dose to be administered, in order to limit the amount of freely circulating active agent, which could lead to equally severe adverse effects.

Abbreviations: CFD, computational fluid-dynamics; DEM, discrete element method; JKR, Johnson-Kendall-Roberts; SANT, shear-activated nanotherapeutics; SD, Stokesian dynamics; SIMPLE, semi-implicit method for pressure linked equations; WSS, wall shear stress.

To address this challenge, a number of targeted drug delivery strategies has been devised,[3] including liposomes encapsulating tPA and undergoing rupture as a response to an external ultrasound source,[4] magnetic microrods mechanically disrupting the clot under the action of an external magnetic field,[5,6] carriers made of microbubbles covered by magnetic nanoparticles with responsiveness to both the magnetic field and ultrasound solicitation,[7] polymer particles encapsulating magnetite and tPA,[8] and core–shell fibrin-specific colloidal hydrogels.[9]

However, all such approaches require rather precise knowledge of the clot position and an external activation mechanism. In this context, a promising drug targeting method has been proposed by Korin et al,[10] and it is based on the so-called shear-activated nanotherapeutics (SANTs). The drug carrier is here constituted by micrometric clusters of polymeric nanoparticles coated with the active agent. These clusters are stable under normal blood flow conditions but can be designed to undergo breakup right onto the clot, in response to the local increase in the hydrodynamic stress caused by the lumen restriction.[11,12] The resulting fragments experience a lower drag force with respect to the parent aggregate and therefore are more likely to adhere to the clot and perform the thrombolytic action, as observed by Korin et al.[10] This biophysical strategy benefits from the narrowing of the lumen diameter and from the consequent local increase in the shear stress, which occurs regardless of the specific cause or location of the clot, thus offering a robust and broadly applicable targeting method.

The refining of the delivery strategy SANTs relies upon asks, however, for demanding and challenging in vivo and/or in vitro experimental trials. In this context, numerical simulations can provide valuable insights into the blood flow dynamics, which can be useful in tuning the properties of the drug carrier. Computational fluid dynamics (CFD) simulations, for instance, have been successfully used to predict wall shear stress distribution in aortic vessels, accurately reconstructed by magnetic resonance imaging,[13] and simulations on model representations of obstructed vessels elucidated the role that the blood flow field distortion has on platelet aggregation and clot formation.[14] Cardiovascular research has also used CFD to predict how hemodynamics changes as a result of pathology,[15] surgical outcomes,[16,17] or to design artificial medical devices.[14]

However, to properly tune SANTs, the investigation of the flow characteristics is not sufficient, as insights into the mechanical response of the drug carrier to the fluid dynamic stress are also required.[11,12,18] A detailed simulation of the behaviour of aggregates immersed in a flow field can be obtained by discrete element method (DEM) simulations. DEM simulations allow one to track the motion of each single particle composing the carrier aggregate, taking into account both the adhesive interaction between the primary particles and the interaction with the surrounding fluid.[19–21] Different degrees of complexity can be introduced in DEM simulations when modelling the fluid dynamics interactions between the suspending fluid and the solid particles. In the so-called free-draining approximation, each particle is assumed to experience the Stokes drag force, as if no other particle were in the flow.[22] However, the hydrodynamic screening effects taking place in the agglomerate are known to play a non-negligible role.[23] These can be accurately taken into account by Stokesian dynamics, for instance,[24] which, by using a low-order expansion of the exact solution of the flow field, is able to compute the hydrodynamic forces acting on each particle. This allows one to predict, for instance, particle aggregation,[25] agglomerate restructuring, and the breakup of soft and rigid agglomerates in both simple flow configurations,[26–29] and in the complex flow field.[30]

The present work investigates the mechanical response of three potential drug carrier morphologies to the pathological flow field stress typically encountered in obstructed blood vessels. CFD simulations are used to investigate the effect of an obstruction in three geometries mimicking a clot-obstructed vessel (an axisymmetric obstructed vessel, an asymmetric obstructed vessel, and a microchannel model of stenosis) and to compute a dataset of cluster trajectories. Instead, DEM simulations based on Stokesian dynamics are used to accurately evaluate the stresses acting on the particle–particle bonds and to finally predict the occurrence of breakup in the obstruction. The results herein presented can be used for setting up an in vitro experimental campaign aimed at establishing SANTs as a robust targeting strategy to address clot lysis.

2 | METHODS

The system under investigation is made up of micrometric drug carriers dispersed in a fluid flowing in an obstructed vessel. The fluid flow field was computed by CFD simulations, whereas DEM simulations based on Stokesian dynamics have been used to investigate the mechanical response of three model drug carriers. The simulated fluid is Newtonian and incompressible, and its flow regime is assumed to be laminar. Indeed, blood is a non-Newtonian fluid, composed of a continuous plasma matrix and a dispersed phase, which includes red blood cells, white blood cells, and platelets. This particular composition leads to a shear-thinning rheological behaviour, which has been described by resorting to a plethora of non-Newtonian models.[31–33] However, especially in

large vessels, the common assumption of a Newtonian behaviour was seen to be sufficiently accurate.[34] Given the small dimensions of clusters, their influence on the flow field was neglected, and they were assumed to behave as tracer particles carried passively by the flow field.

2.1 | Prediction of the flow fields

The steady–state flow–field was computed by ANSYS Fluent 20. Based on a finite volume approach, the code solves the following continuity and momentum transport equations:

$$\nabla \cdot u = 0 \tag{1}$$

$$\rho \frac{\partial u}{\partial t} + \rho \nabla \cdot (uu) = -\nabla p + \nabla \tau \tag{2}$$

where u is the velocity of the fluid, ρ is the fluid density, p is the pressure, and τ is the viscous stress tensor. Pressure and velocity were coupled by using the SIMPLE algorithm. The viscosity was set to 10^{-3} Pa · s, and the density to 1000 kg/m^3.

The geometries of the investigated systems are shown in Figure 1. Although clots in stenotic vessels come in a variety of shapes and sizes, axisymmetric or asymmetric deformed cylindrical tubes have been frequently employed as model representations,[35–38] and thus these two geometries have been investigated in this work, alongside the reproduction of a microfluidic device designed and operated in such a way as to reproduce pathological blood flow conditions.

The axisymmetric geometry (Figure 1A) models the artery as a cylinder (diameter 1.12 mm), while the shape of the stenosis is described by a sinusoidal curve.[36] In the asymmetric geometry (Figure 1B), the pre-stenotic region is equal to the one from the previous case, but the shape of the clot is instead described by a semi-ellipse,[38] having a major axis of 2.24 mm and a minor axis of 1.015 mm. The major axis of the semi-ellipse is aligned with the flow direction, and the obstruction in the blood vessel is obtained by extruding the semi-ellipse in the orthogonal direction. The microfluidic device (Figure 1C) has a rectangular section, and it is formed by a central stenotic tract (95 μm high x 400 μm wide x 10 mm long) and by a pre- and post-stenotic tract (each: 495 μm high x 2 mm wide x 5 mm long). The three vessels present a 95% lumen obstruction.

In all geometries, the flow travels a distance in the pre-stenotic region that is sufficient to reach the condition of fully-developed flow at the stenotic region entrance. The flow-rate was adjusted according to a trial and error procedure until pathological values of the shear stress were reached in the restricted region (order of magnitude is 10^2 Pa). A uniform velocity profile has been set at the inlet of the axisymmetric and the asymmetric stenosis. In the microchannel, we prescribed instead a pressure difference between the inlet and outlet to better reproduce the operative conditions that would be encountered in an actual experimental apparatus: the fluid would be fed to the microchannel through cylindrical tubes linked to its upper part, thus not achieving a uniform velocity profile at the inlet of the vessel. Wall boundary conditions were applied on the lateral surfaces, and an outflow boundary condition was imposed at the outlet. The simulation domain was subdivided using 139 375 hexahedral cells, 157 330 tetrahedral cells, and 98 720 hexahedral cells for the axisymmetric vessel, the asymmetric vessel, and the microfluidic device, respectively. Given their small dimension and inertia, the clusters follow the streamlines of the fluid very closely and thus can be treated as tracer particles. Hence, by
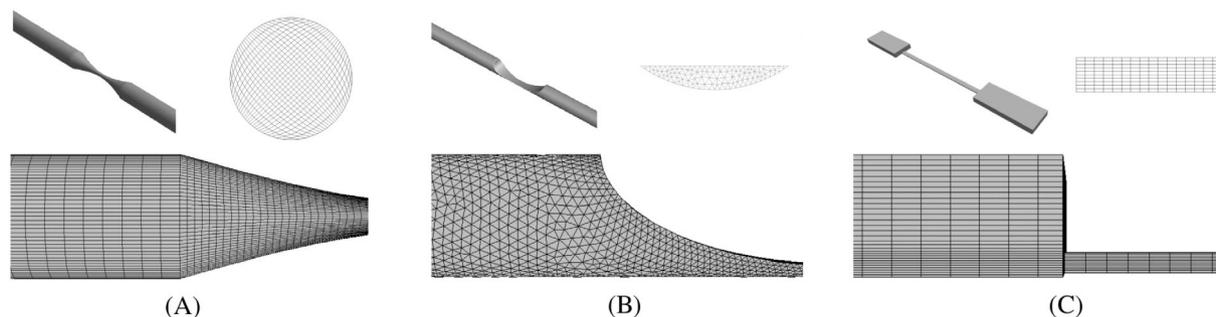

FIGURE 1   (A) Geometry, mesh detail, and minimum cross-section shape for the axisymmetric stenosis, (B) the asymmetric stenosis, and (C) the microchannel. The minimum cross-section of the axisymmetric stenosis is a circle with a diameter equal to 220 μm. The minimum cross-section of the asymmetric stenosis is a circular segment, and its height is 105 μm. The minimum cross-section of the microchannel is a rectangle with sizes of 95 μ and 400 μm

integration of the fluid velocity, we computed a set of tracer particle trajectories in order to evaluate the hydrodynamic stress time series clusters are subjected to, which can, in turn, be used to evaluate the cluster internal stresses by discrete element method simulations.

2.2 | Drug carrier morphologies

The three types of aggregate morphologies shown in Figure 2 have been taken into consideration in this work: porous isostatic aggregates, spherical random close packing (RCP), and hollow aggregates. Porous aggregates are generally obtained from destabilized colloidal suspensions, under mild stirring or in a diffusion-controlled aggregation process. In this work, numerical reproductions of such aggregates were generated by using a tunable cluster–cluster algorithm able to generate isostatic structures with a prescribed fractal dimension.[39] Starting from a population of trimers, the algorithm generates larger aggregates from the collision between equally sized aggregates. In each aggregation event, a single new bond is formed, thus keeping the structure isostatic. In such aggregates, the failure of a single bond causes the breakup of the cluster and the generation of two fragments. To obtain statistically robust results, we adopted a population made of 100 different aggregates, each made of 96 primary particles with a fractal dimension $d_f = 1.8$. Their outer diameter is around 3.8 μm.

Spherical aggregates of therapeutic nanoparticles can be obtained via a spray-drying process. In this process, the Péclet number plays a major role in the final morphology.[40,41] When the operating conditions are such that the diffusion of the particles inside a droplet is faster than the droplet shrinkage, the concentration of particles inside the droplet is kept homogeneous throughout the process, and the final cluster is compact. On the contrary, when the droplet shrinkage is fast, an accumulation of particles at the periphery of the droplet occurs, which finally leads to the generation of hollow aggregates with an external crust made by contacting particles locked in

place by van der Waals forces. Numerical twins of the compact spherical aggregates have been here generated using the RCP algorithm proposed by Skoge and coworkers,[42] which arranges particles in such a way as to minimize the void fraction inside the aggregate (around 36%), avoiding, at the same, time the formation of an ordered structure. The obtained aggregate is, in this case, hyperstatic, that is, the breakup of a single bond does not lead to the failure of the structure. A population of 20 different clusters made of 200 primary particles and with a diameter of 1.5 μm was here investigated.

Hollow aggregates were generated from compact RCP aggregates by removing internal primary particles while keeping intact the outer shell and preserving the hyperstatic nature of the aggregate. We produced aggregates for which $R_{min}/R_{max} = 0.8$, where R_{min} is the distance between the centre of mass of the aggregate and the closest monomer, whereas R_{max} is the distance between the centre of mass of the aggregate and the farthest monomer. A population of 40 different clusters made up of 350 primary particles and with a diameter of approximately 2.3 μm was investigated. All clusters were made up of spherical primary particles with radius $a = 100$ nm, elastic modulus $E = 3.4$ GPa, Poisson's ratio $\nu = 0.35$, and surface energy $\gamma = 0.004$ J/m^2.

2.3 | Discrete element method (DEM)

DEM simulations built upon Stokesian dynamics have been performed to evaluate the stress distribution inside the clusters and to study their breakup behaviour. As previously pointed out, the size of the aggregates is small compared to the typical distances over which the variation of the velocity gradients takes place. Therefore, we assumed that aggregates experience a linear flow field, with uniform velocity gradients, which can be well approximated by the velocity gradients obtained by tracking a set of tracer particles. As a consequence, in a reference frame moving with the agglomerate, the undisturbed velocity at the position occupied by
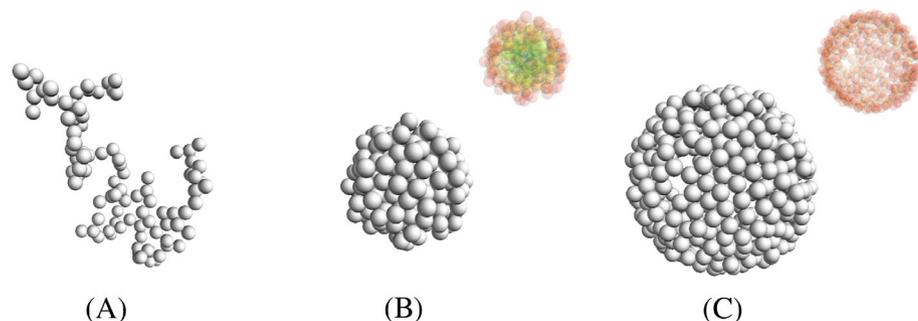

FIGURE 2 Samples of the simulated aggregates: (A) isostatic, (B) random close packing, and (C) hollow spherical aggregates. The colourmap shows the rear half of the clusters to highlight the difference between the compact core of the random close packing (RCP) aggregates and the empty core of the hollow aggregates. Green primary particles are close to the centre of mass of the aggregate, whereas red primary particles are far from it.

any monomer composing the cluster can be computed as $u_m^\infty(x) = \nabla u^\infty \cdot x_m$, where ∇u^∞ is the velocity gradient tensor evaluated at the position of the centre of mass of the agglomerate and x_m is the position vector of the m-th monomer with respect to the centre of mass of the aggregate.

Under the condition of a vanishingly small particle Reynolds number, it is possible to evaluate the hydrodynamic forces and torques acting on each monomer of the cluster by resorting to Stokesian dynamics. This method, employed here in the force-torque-stresslet formulation, provides the relation between hydrodynamic force and torque and the relative velocity of the monomers compared to the velocity of the undisturbed flow at the monomer position. The relation between such quantities is given by the following linear system of equations[24]:

$$\frac{1}{\mu}\begin{bmatrix} M^{UF} & M^{UT} & M^{US} \\ M^{\Omega F} & M^{\Omega T} & M^{\Omega S} \\ M^{EF} & M^{ET} & M^{ES} \end{bmatrix}\begin{Bmatrix} F \\ T \\ S \end{Bmatrix} = -\begin{Bmatrix} u - u^\infty(x) \\ \omega - \omega^\infty \\ -E^\infty \end{Bmatrix} \quad (3)$$

where $u = (u_1, ..., u_m, ..., u_{n_m})$ and $\omega = (\omega_1, ..., \omega_m, ..., \omega_{n_m})$ are the vectors of the linear and angular velocities of the monomers composing the agglomerate, respectively ω^∞ is the angular velocity of the undisturbed flow field; and $u^\infty(x)$ is the linear velocity of the undisturbed flow at the monomer position. The quantities $F = (f_1, ..., f_m, ..., f_{n_m})$ and $T = (t_1, ...t_m, ..., t_{n_m})$ are, respectively, the hydrodynamic force and torque acting on the monomers. Forces, torques, and velocities are three-component vectors, whereas the rate-of-strain tensor, and the stresslet tensor that are symmetric and traceless, are conveniently reduced to the equivalent five-component column vectors $E^\infty = (e_1, ..., e_m, ..., e_{n_m})$, where for each monomer $e_m = \left(e_{xx}^\infty - e_{zz}^\infty, 2e_{xy}^\infty, 2e_{xz}^\infty, 2e_{yz}^\infty, e_{yy}^\infty - e_{zz}^\infty\right)$, and $S = (s_1, ...s_m, ..., s_{n_m})$, where $s_m = (s_{m,xx}, s_{m,xy}, s_{m,xz}, s_{m,yz}, s_{m,yy})$. The matrix in Equation (3) is called the mobility matrix, and it is here used in its far-field formulation, with no lubrication correction applied, as aggregates are rigid assemblies and no relative motion between the primary particles occurs.[43]

By applying the condition of rigid body motion to the aggregate, the hydrodynamic force and torque acting on each primary particle can be calculated from Equation (3). As a subsequent step, it is possible to estimate the contact forces and torques between the monomers of the clusters within the limit of elastic deformations. The normal (i.e., tensile) force acting between two primary particles is obtained by linearization of the Johnson-Kendall-Roberts (JKR) theory of contact mechanics,[44] whereas tangential force, bending moment, and torsional moment are

predicted by the models by Dominik and Tielens[45] and Marshall.[46] In this way, the distribution of the hydrodynamic force exerted by the fluid on the primary particles is translated into a distribution of internal stresses acting at the contact region between each pair of primary particles. The method is illustrated in detail in the work by Vanni.[27]

3 | RESULTS AND DISCUSSION

We have characterized the fluid dynamics and computed the viscous stress distributions in the two realistic reconstructions of clot-obstructed vessels and in the microfluidic device, verifying that the latter is able to reproduce the pathological stress conditions generated by a clot. Then, using DEM simulations, we studied the tensile stress distribution in three different types of drugs exposed to the fluid dynamic stress to finally identify the expected breakup mechanism.

3.1 | CFD–axisymmetric stenosis

First, transient simulations of the flow field in the vessel have been conducted. The flow field was seen to quickly reach a stationary solution, so steady-state simulations have been used in the following to characterize the fluid dynamic behaviour of the obstructed vessels. Simulations have been conducted, varying the velocity at the inlet and monitoring the peak value of the wall shear stress. The results are summarized in the plot shown in Figure 3A. As expected, the peak value of the wall shear stress increases with the inlet velocity. However, the increase was seen to not be linear with the inlet velocity. This was seen to be due to the generation of vortices, which appeared in the post stenotic region for any value of the inlet velocity larger than 0.02 m/s (corresponding approximately to a Reynolds number equal to 200).[36] The generated vortices can be observed in Figure 3B. The obstruction, therefore, causes a recirculation in the post-stenotic region, which is considered to be beneficial for the action of SANTs,[10] as it keeps the fragments generated upon breakup near the wall of the stenotic regions, thus increasing the probability of adhesion to the clot. Smaller fragments experience, in fact, larger adhesion forces compared to the drag forces, and thus they are most likely to adhere to the walls of the vessels compared to the larger parent aggregate.

As reported by Korin and coworkers,[10] wall shear stress greater than 100 Pa should be considered pathological. Therefore, the simulations for which the maximum wall shear stresses are equal to 125 and 183 Pa, respectively, have been used to compare the fluid dynamic

behaviour in the three vessels. Figure 4 reports velocity and stress profiles at the beginning, centre, and end of the stenotic region for an inlet velocity of 0.10 m/s. It can be seen that the fluid reaches a peak velocity of 0.20 m/s in the pre-stenotic region and a peak of 3.62 m/s in the stenotic region. As apparent from the velocity profile after the restricted section (at $Z = +2.2D$), the fluid generates a slowly decaying central jet surrounded by two lateral vortices. The shear stress profile of Figure 4B makes it apparent
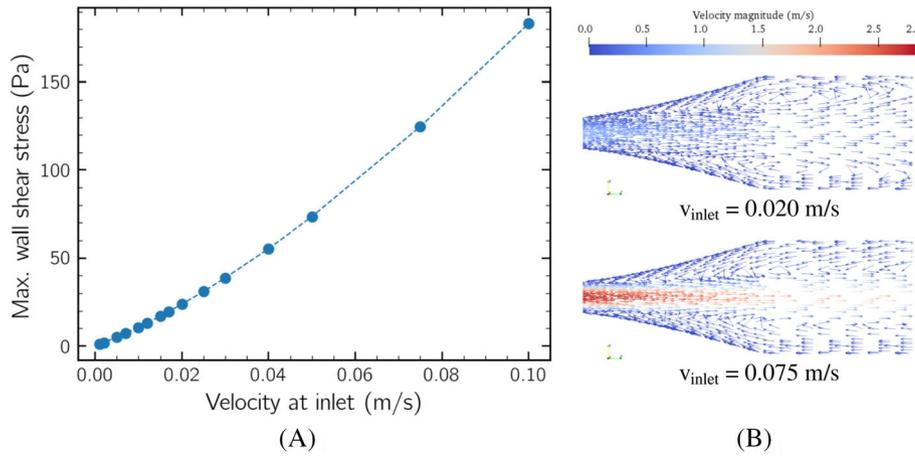
FIGURE 3 (A) Effect of the inlet velocity on the peak value of the wall shear stress in the axisymmetric stenosis. (B) Velocity vectors in the axisymmetric stenosis for two values of the inlet velocity
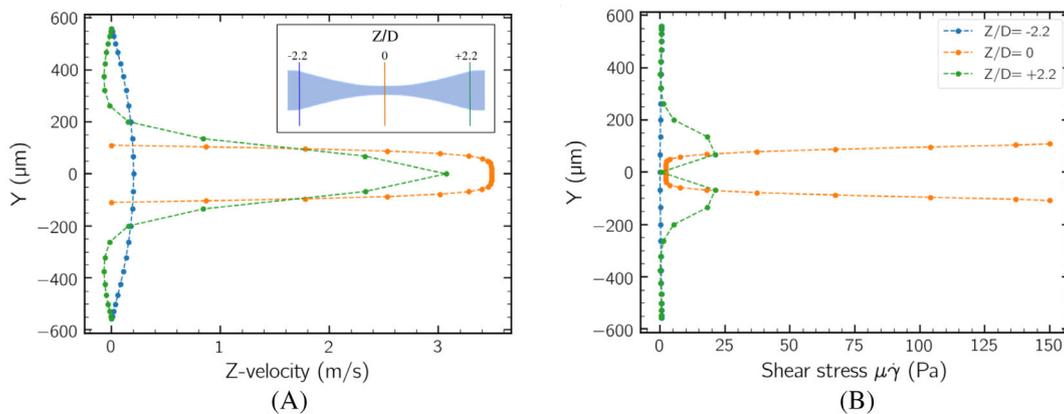
FIGURE 4 Axisymmetric stenosis flow field. (A) Z-velocity and (B) $\mu\dot{\gamma}$ profile along the Y-coordinate at three different Z-coordinates. $Z/D = -2.2$ is the beginning of the stenotic section, $Z/D = 0$ is its middle point, and $Z/D = +2.2$ is its end.
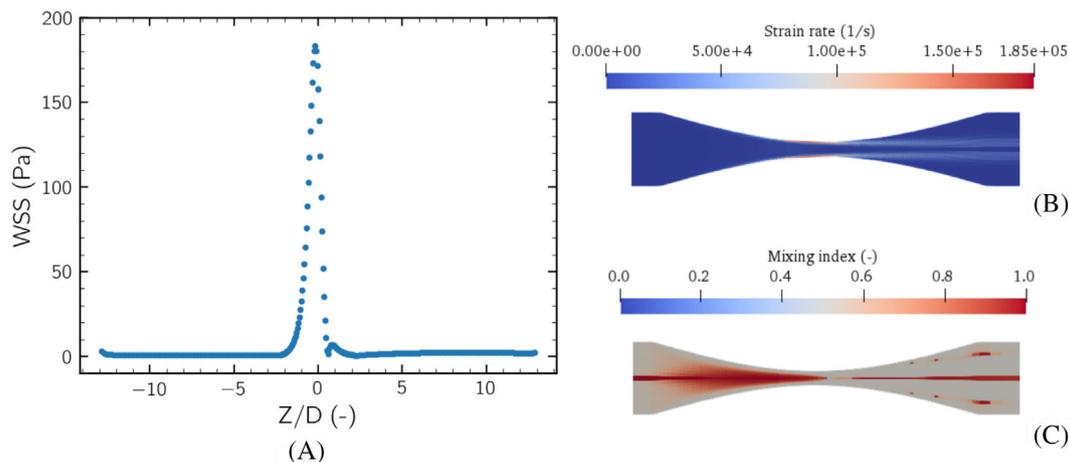

FIGURE 5 Axisymmetric stenosis flow field characterization for an inlet velocity of 0.1 m/s. (A) Axial profile of the wall shear stress. (B) Contour plot of the strain rate and (C) mixing index in longitudinal cross-section. WSS, wall shear stress

that the largest shear stresses are present in the restricted section, and they are located in the region closest to the wall.

The effect of the restriction on the shear stress distribution is made more apparent in Figure 5A, where the maximum wall shear stress is plotted as a function of the longitudinal coordinate. The stress at the wall increases from about 0.4 Pa before the obstruction to a maximum of 183 Pa on the restricted section. The distribution of the strain rate is shown in Figure 5B. It can be noticed that the region of highest strain rate is located close to the wall in the converging and central region of the vessel, and it moves closer to the centre-line in the diverging region, at the transition between the fluid jet and the recirculation zones, thus suggesting that this region could contribute, even if to a lesser extent, to the breakup of the suspended drug carriers.

In addition to the strain rate, the flow field has been locally characterized also by the mixing index λ, calculated as:

$$\lambda = \frac{\dot{\gamma}}{\dot{\gamma} + \widetilde{\omega}} \qquad (4)$$

where $\widetilde{\omega}$ is the vorticity of the flow field and $\dot{\gamma}$ is the shear rate. For $\lambda \rightarrow 0$, the flow field is predominantly rotational; for $\lambda \rightarrow 1$, it has a strong elongational component; and for $\lambda \simeq 0.5$, the flow is in a condition of simple shear, that is, the rotational and the elongational components equally contribute to the flow field. As made apparent by the contour plot of λ reported in Figure 5C, even if the stenosis causes a local increase in the elongational component of the flow, in the regions where the largest stresses are observed, the value of the mixing index is around 0.5, thus indicating that pure shear flow conditions are present in the region of the largest shear stress.
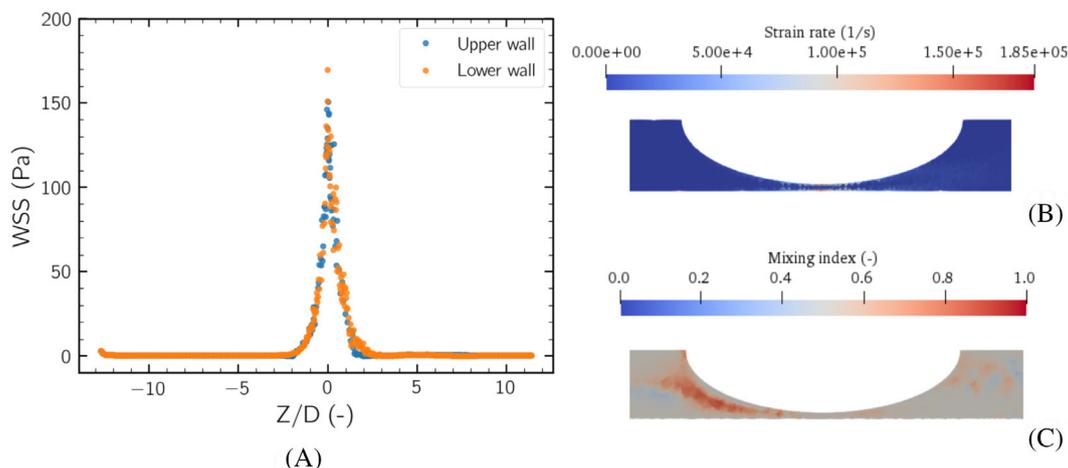
3.2 | CFD–asymmetric stenosis

Similarly to what has been done for the axisymmetric vessel, we ran different simulations at varying inlet velocity in the asymmetric vessel in order to determine the conditions leading to pathological wall shear stress (125 and 183 Pa). These have been found for an inlet velocity of 0.051 and 0.067 m/s, respectively. Figure 6A shows the distribution of the wall shear stress for the upper and lower walls of the vessel. It can be seen that the largest shear stress appears again in the restricted section, with no remarkable difference between the upper and lower walls. The mixing index and strain rate distributions reported in Figure 6B,C show that the flow field is mostly shear-dominated in the region of large shear stress, with elongational components of the flow arising only in the small regions before and after the restriction.

In Figure 7, we report the velocity profile and the shear stress profile on three different sections. In the plot (A), it can be seen that the fluid reaches a peak velocity of 0.13 m/s in the pre-stenotic region and a peak of 2.2 m/s in the stenotic region. The negative values of the velocity at $Z/D = 2.0$ show that, also, in this case, a recirculation pattern establishes in the post-stenotic region. Such a behaviour was seen to emerge at a Reynolds number greater than 200. The stress profile $\mu\dot{\gamma}$ for three different Z-coordinates is reported in Figure 7B. Also, in this case, the maximum shear stress is observed near the walls of the vessel in the restricted region.

3.3 | CFD–Microchannel model of stenosis

A CFD characterization of the microfluidic device has been conducted in order to find the operating conditions

(A)

(B)

(C)

FIGURE 6 Asymmetric stenosis flow field characterization for an inlet velocity of 0.067 m/s. (A) Axial profile of wall shear stress on the upper and lower wall. Contour plot of (B) shear rate and (C) mixing index in the symmetry plane. WSS, wall shear stress

that better reproduce the fluid dynamic behaviour of the stenotic vessels. Pathological shear stresses (125 and 183 Pa) were reached for a volumetric flow-rate of around 1.10 and 1.50 ml/min, respectively.

The profiles of Z-velocity and $\mu\dot\gamma$ before the restricted section, in the middle, and after the restricted section are reported in Figure 8. Similarly to the stenotic vessels, a recirculation pattern appears at the end of the restricted section (plot A), thus proving that the fluid dynamic behaviour of the microfluidic device well compares with that of the stenotic vessels. In Figure 8B, we report the shear stress profiles in the microchannel. The peak value of wall shear stress is due to the strong deformation of the flow field at the entrance of the restricted section, and it is reached at the very beginning of the stenotic region. Figure 9 makes this feature more apparent. The figure shows the strain rate and mixing index contour plots on the symmetry plane of the microchannel (B and C), and the profile of wall shear stress along Z on the same plane (A). It can be seen that the peak value of

183 Pa of the shear stress is reached at the bottom wall of the device, soon after the beginning of the restricted section, and then it reaches a plateau value equal to 95 Pa. The mixing index distribution shows that the flow is shear-dominated and elongation is only present in the pre- and post-stenotic regions, as observed in the stenotic vessels.

Finally, we report in Table 1 the main properties of the flow field in the three investigated geometries, from which one can notice that different flow-rates are needed to reach the same pathological wall shear stress in the three systems.

3.4 | Discrete element method (DEM)

The mechanical response of the agglomerates to the viscous stress was computed by running Stokesian dynamics simulations along the trajectories obtained via the interpolation of the flow field. Given the small size of the
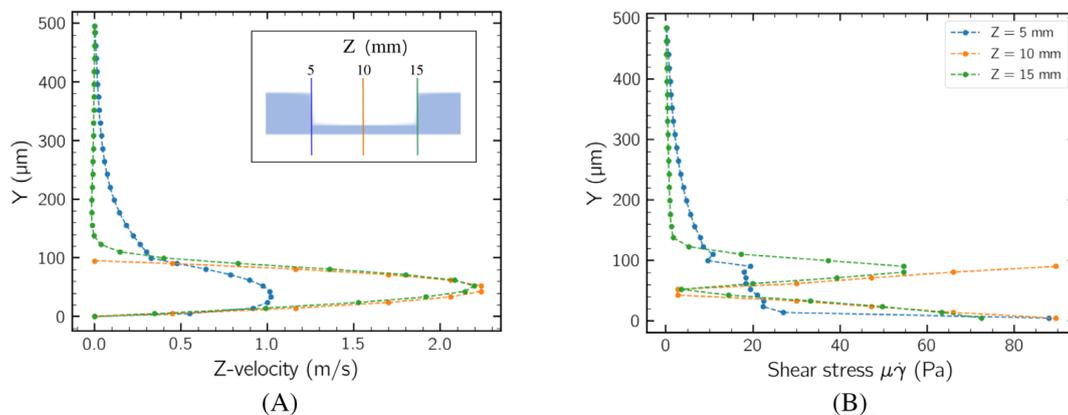

FIGURE 7 Asymmetric stenosis flow field. (A) Z-velocity and (B) $\mu\dot\gamma$ profile along the coordinate Y at three different coordinates $Z \cdot Z/D = -2.0$ is the beginning of the stenotic tract, $Z/D = 0$ is its middle point, and $Z/D = +2.0$ is its end
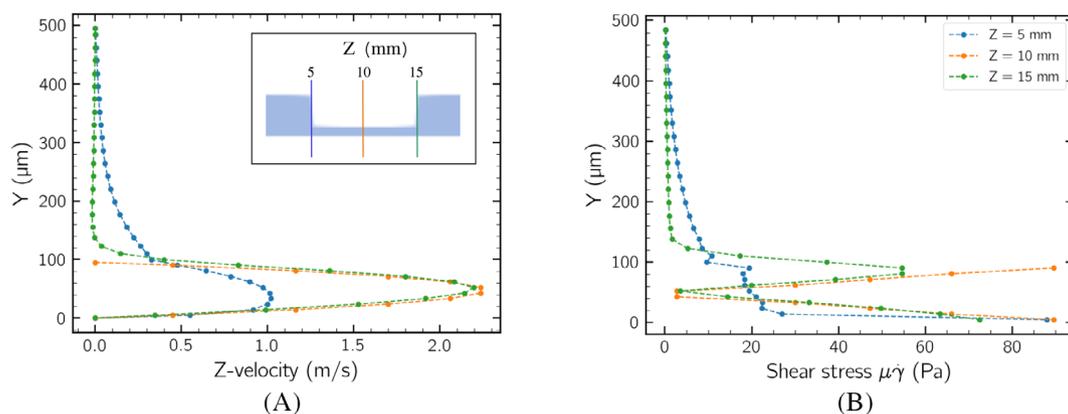

FIGURE 8 Microchannel flow field. (A) Z-velocity and (B) $\mu\dot\gamma$ profile along the coordinate Y at three different coordinates Z. $Z = 5$ mm is the beginning of the stenotic tract, $Z = 10$ mm is its middle point, and $Z = 15$ mm is its end
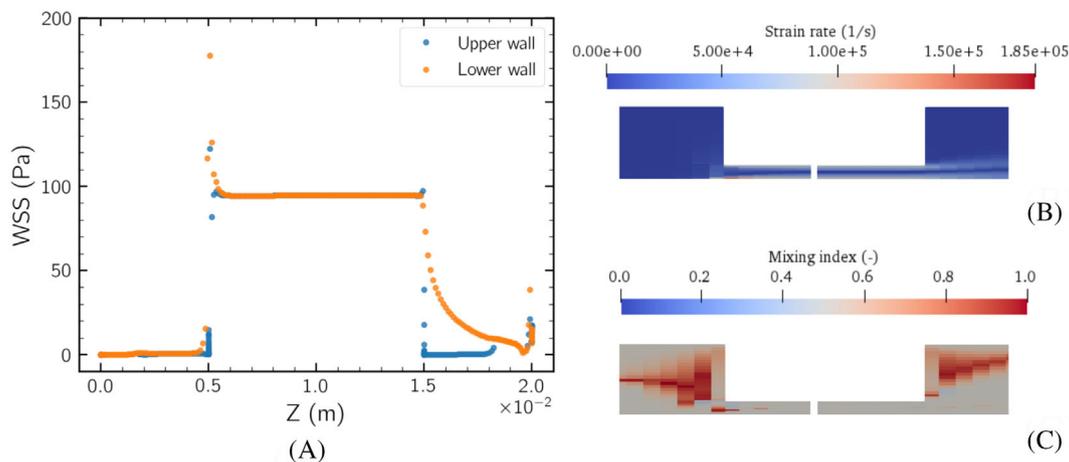
FIGURE 9 Microchannel flow field characterization for an inlet flow-rate of 1.50 ml/min. (A) Axial profile of wall shear stress on the upper wall and the lower wall. Contour plot of (B) strain rate, and (C) mixing index on the symmetry plane. WSS, wall shear stress

TABLE 1 Principal properties of the flow field for the highest flow-rate for the three geometries

Stenosis	Region	Flow-rate (ml/min)	Maximum velocity (m/s)	Hydraulic radius (µm)	Re
Axisymmetric	Pre-stenotic	5.90	0.20	280	223
	Stenotic		3.62	55	794
Asymmetric	Pre-stenotic	3.96	0.14	280	156
	Stenotic		2.21	35	300
Microchannel	Pre-stenotic	1.50	0.09	200	63
	Stenotic		2.24	40	357

FIGURE 10 Drag forces (above) and normal stresses at intermonomer bonds (below) for a cluster–cluster fractal aggregate (left) and random close packing (RCP) aggregate (right) under a flow with shear rate dv_x/dy
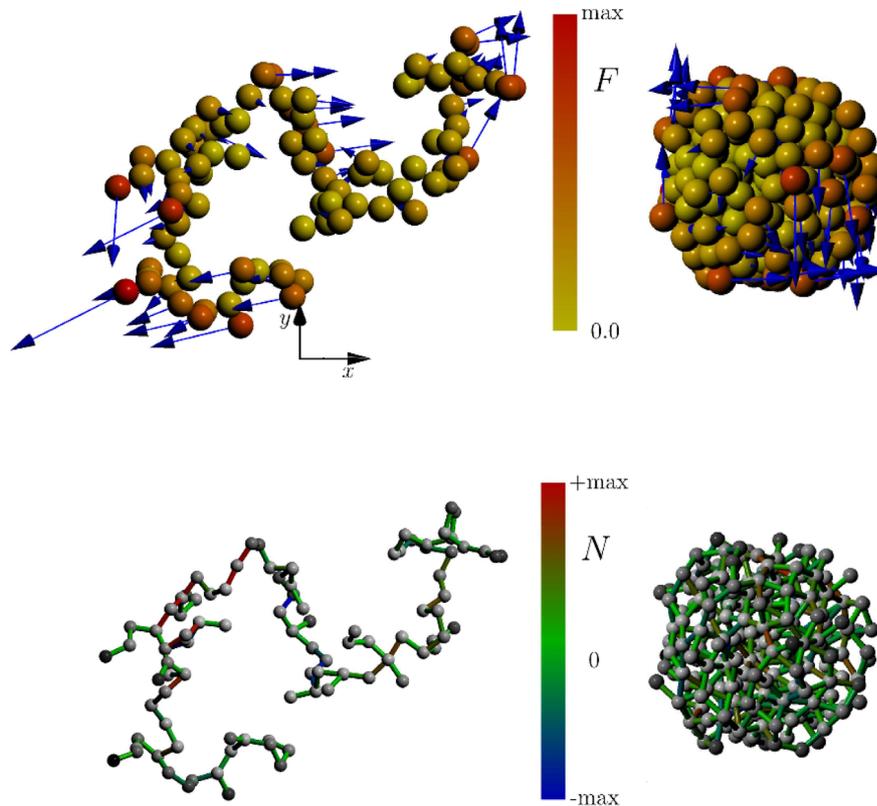
clusters, trajectories have been computed using a one-way coupling, neglecting the back reaction of the clusters on the fluid and the binary interaction between them. By Stokesian dynamics, we have been able to translate shear rate signals into tensile stress acting on each particle–particle bond. As an example, Figure 10 illustrates the outcome of the method for two of the aggregates investigated in this work (a fractal cluster–cluster [CC] aggregate and a random close packing [RCP] spherical aggregate) when immersed in a pure shear flow with $\dot{\gamma} = dv_x/dy$. The upper images show the drag forces acting on each primary particle of the aggregate, whereas the lower ones report the normal (i.e., tensile) forces acting at inter-particle contacts. It is worth remembering that, for fragile aggregates, breakup takes place when the tensile normal stress exceeds the cohesive strength at a contact, and, consequently, the normal stress is the fundamental variable to predict the occurrence of breakup. Although subjected to the same flow field, the distribution of the normal stress in the two aggregates is very different, as made more clear by Figure 11. In the compact and strongly hyperstatic RCP aggregate, the strength of the normal force is small in comparison to what can be observed in the porous CC aggregates, where stresses are accumulated along filaments and can reach very high values. It is apparent, therefore, that the stresses acting on the aggregates depend on both the local strain rate and the geometry of the aggregates. If the microchannel has to be a reliable reproduction of the stenotic system, a similar distribution of the strain rate has to be obtained, so that two aggregates of the same kind are subjected to the same stress.

In Figure 12, we report a sample strain rate signal and the maximum instantaneous tensile stress N_{max} acting in an isostatic cluster. The maximum normal stress is normalized using $6\pi\mu a\langle u\rangle$, where $\langle u\rangle$ is a representative velocity of the fluid (mean velocity in the stenotic region of the microchannel, 1.1 m/s). It is worth noting that there is no time lag between the two signals. This is due to the fact that aggregates are considered perfectly rigid, and hence the transmission of the stress from the flow field to the agglomerate structure occurs instantaneously. The fluctuating behaviour of N_{max} has instead to be ascribed to the rotation of the cluster in the flow field.

The higher the strain rate is, the more intense the hydrodynamic forces acting on clusters are; therefore, the maximum value of strain rate along a trajectory γ_{max} can be used as a parameter to compare the effectiveness of the different vessel geometries in inducing breakup. A statistical analysis on the maximum shear rate experienced by aggregates flowing in the three vessels is presented in Figure 13. The plot reports the cumulative distribution function (CDF) of the peak value of strain rate experienced by the agglomerates along trajectories in
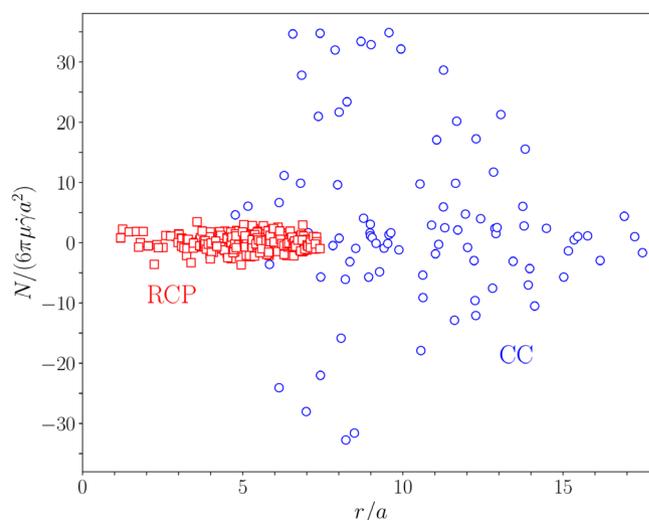

FIGURE 11 Normal stress at the bonds of the aggregates of Figure 10 as a function of the distance r from the centre of mass of the aggregate. RCP, random close packing; CC, cluster-cluster aggregate
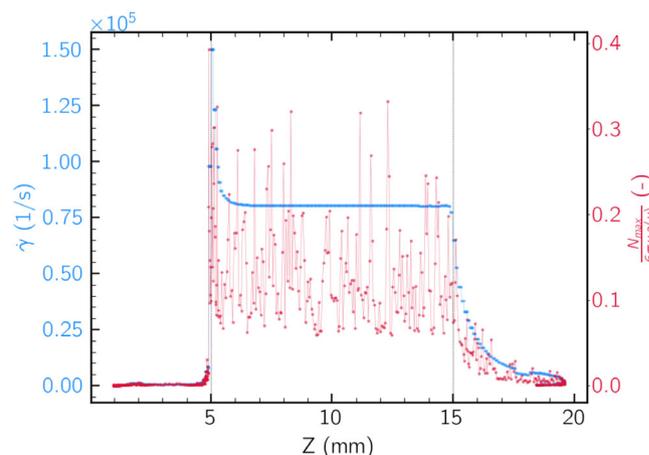

FIGURE 12 Strain rate $\dot{\gamma}$ (blue) and normalized maximum tensile stress N_{max} inside an isostatic cluster (red) along the Z-coordinate for a sample trajectory in the microchannel. The fluctuating behaviour of N is due to changes in the orientation of the cluster with respect to the flow field

the three geometries for a maximum wall shear stress of 125 and 183 Pa, respectively. It can be seen that the shear rate statistics acting on the clusters in the microchannel well compares with the one experienced by the clusters in the obstructed vessels, thus proving our microfluidic device as a valid representation of an obstructed blood vessel and a valid setup for running experimental trials. The longer restricted section of the microchannel in comparison to the stenotic systems has no impact on the distribution of $\dot{\gamma}_{max}$, but it is expected to facilitate the separation of the fragments after breakup.

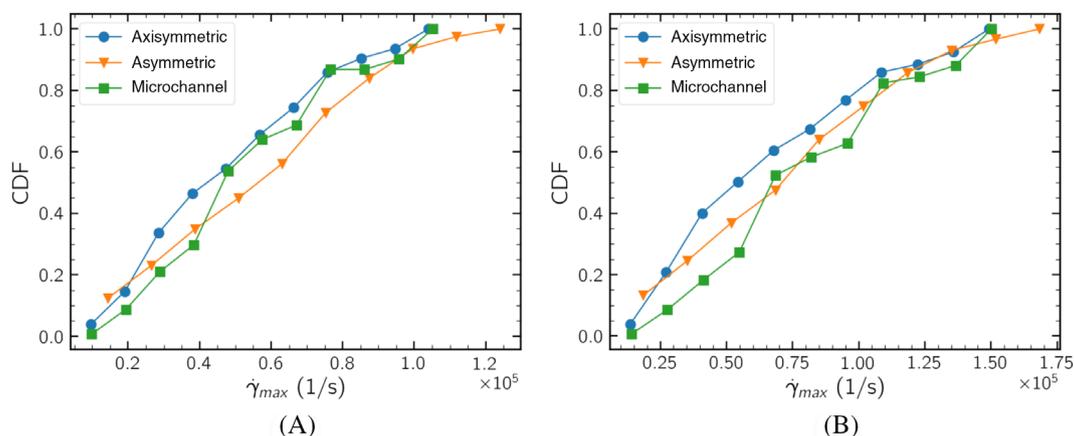Finally, we studied the mechanical response of different kinds of clusters to the hydrodynamic solicitation.

FIGURE 13   Cumulative distribution functions (CDF) of the maximum strain rate $\dot{\gamma}_{max}$ along trajectories; circles represent the axisymmetric stenosis, triangles represent the asymmetric stenosis, and squares represent the microchannel. (A) Maximum wall shear stress $= 125$ Pa. (B) Maximum wall shear stress $= 183$ Pa
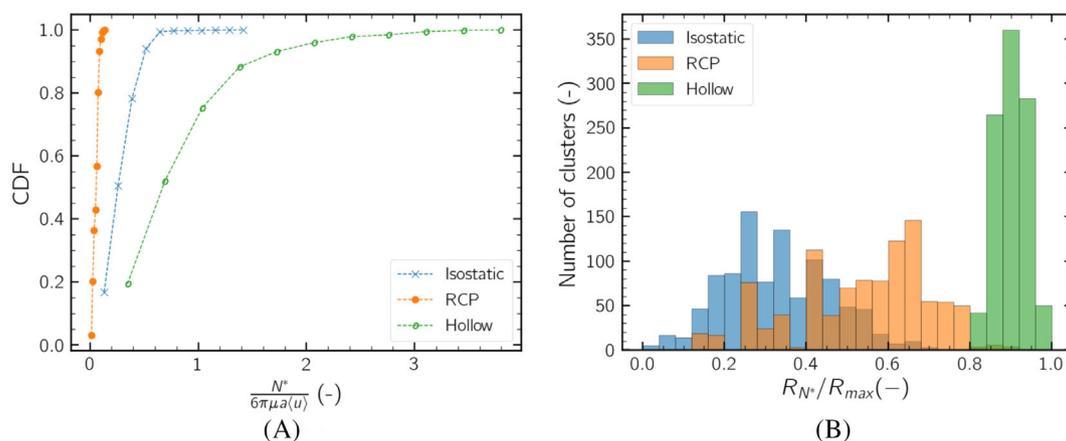

FIGURE 14   (A) Cumulative distribution functions (CDF) of the maximum normal stress inside clusters flowing in the microchannel. Crosses represent isostatic clusters, full circles represent random close packing (RCP) clusters, and empty circles represent hollow clusters. (B) Relative position of the most solicited bond in 1000 isostatic clusters, 1000 RCP clusters, and 1000 hollow clusters

Figure 14A reports the CDF of $N^* = \max(N_{max})$, that is, the maximum tensile stress experienced by a cluster along its entire trajectory in the microchannel. From the plot, it can be noted that the RCP clusters emerged as the most resistant class of clusters, while hollow aggregates emerged as the weakest one. Isostatic clusters showed an intermediate behaviour.

Figure 14B reports the position of the most solicitated bond for every cluster. R_{N^*} is the distance of the most solicitated bond from the centre of mass, normalized by the cluster maximum radius in the plot. The analysis of the distribution of hydrodynamic forces in the aggregate structure showed that for isostatic clusters, hydrodynamic forces are more intense on the outer region of the cluster because there is no shielding from the rest of the structure. However, the produced mechanical stress is propagated from the outer region to the inner part, and

therefore, the highest tensile stresses have been found at the core of the cluster. In such clusters, the breakup of a single bond leads to the collapse of the structure into two fragments. Therefore, the distribution of tensile stress suggests that the generated fragments should be expected to have comparable dimensions. RCP clusters are instead hyperstatic, that is, every primary particle is linked to a large number of particles. For this class of aggregates, we observed that the mechanical stress generated on the outer region is discharged over the neighbouring particles, and it is not propagated and accumulated toward the inner region of the cluster. The highest solicited bonds are thus located in the outer region of the cluster, suggesting that breakup should lead to the detachment of small fragments from the outer surface of the cluster. The distribution of mechanical forces inside the hollow clusters is similar, but the distance over which stresses are

propagated is limited by the shell-shape of the cluster. In this case, therefore, the breakup of outer bonds should be expected to lead to the opening of the shell structure.

4 | CONCLUSIONS

Recently, SANTs have been proposed as an interesting option to address targeted drug delivery in clot-obstructed blood vessels. SANTs are micrometric clusters of polymeric nanoparticles coated with a clot-lysing agent, which are stable under normal blood flow conditions, but they can be designed to undergo breakup right onto the clot, in response to the local increase in hydrodynamic stress caused by the lumen restriction, effectively concentrating the active agent at the point of need.

Motivated by such a delivery strategy, in this work, we investigated the flow field characteristics in obstructed vessels and the mechanical response of three potential drug carriers to the fluid dynamic stresses, in order to prove the feasibility of the SANT approach and to establish a platform for future in vitro experimentations.

CFD simulations of both axisymmetric and asymmetric stenotic vessels have been used to study the flow field and the shear stress distributions typically encountered in ischemic patients. Results showed that the lumen restriction causes a substantial increase in the hydrodynamic stresses, which can be effectively used to induce the breakup of drug carriers. The flow field characterization also made it apparent that after the obstruction, a recirculation pattern takes place, which is considered to be beneficial for the therapeutic action of SANTs. These pathological conditions have been successfully replicated in a microfluidic device with simple and reproducible characteristics.

DEM simulations of aggregates placed in the microchannel flow field have been used to characterize the mechanical response of three different classes of drug carriers. Hollow aggregates emerged as the weakest class of aggregates, RCP aggregates as the most resistant, and isostatic clusters showed an intermediate behaviour. The different resistances and stress distribution inside the cluster structures have been used to infer information about the breakup behaviour.

Such results can be used in future work to guide an experimental campaign aimed at identifying the most suitable carrier structure to be used in addressing normal blood flow restoration in ischemic patients, with the final aim of establishing SANTs as a robust and broadly applicable targeting strategy for addressing clot-lysis.

ORCID

Marco Vanni https://orcid.org/0000-0001-7039-7259
Graziano Frungieri https://orcid.org/0000-0001-8452-5071

REFERENCES

[1] J. Grotta, J. Marler, *Surgical Neurology* **2007**, *68*, S12.

[2] G. D. Graham, *Stroke* **2003**, *34*, 2847.

[3] C. F. Greineder, M. D. Howard, R. Carnemolla, D. B. Cines, V. R. Muzykantov, *Am. J. Hematol.* **2013**, *122*, 1565.

[4] G. J. Shaw, J. M. Meunier, S.-L. Huang, C. J. Lindsell, D. D. McPherson, C. K. Holland, *Thromb. Res.* **2009**, *124*, 306.

[5] J. Hu, S. Huang, L. Zhu, W. Huang, Y. Zhao, K. Jin, Q. Zhu Ge, *ACS Appl. Mater. Interfaces* **2018**, *10*, 32988.

[6] R. Cheng, W. Huang, L. Huang, B. Yang, L. Mao, K. Jin, Q. Zhu Ge, Y. Zhao, *ACS Nano* **2014**, *8*, 7746.

[7] S. Wang, X. Guo, W. Xiu, Y. Liu, L. Ren, H. Xiao, F. Yang, Y. Gao, C. Xu, L. Wang, *Sci. Adv.* **2020**, *6*, eaaz8204.

[8] M. D. Kaminski, Y. Xie, C. J. Mertz, M. R. Finck, H. Chen, A. J. Rosengart, *Eur. J. Pharm. Sci.* **2008**, *35*, 96.

[9] E. Mihalko, K. Huang, E. Sproul, K. Cheng, A. C. Brown, *ACS Nano* **2018**, *12*, 7826.

[10] N. Korin, M. Kanapathipillai, B. D. Matthews, M. Crescente, A. Brill, T. Mammoto, K. Ghosh, S. Jurek, S. A. Bencherif, D. Bhatta, A. U. Coskun, C. L. Feldman, D. D. Wagner, D. E. Ingber, *Science* **2012**, *337*, 738.

[11] M. Soos, L. Ehrl, M. U. Bäbler, M. Morbidelli, *Langmuir* **2010**, *26*, 10.

[12] D. Saha, M. Soos, B. Lüthi, M. Holzner, A. Liberzon, M. U. Bäbler, W. Kinzelbach, *Langmuir* **2014**, *30*, 14385.

[13] R. Perinajová, J. F. Juffermans, J. J. Westenberg, R. L. van der Palen, P. J. van den Boogaard, H. J. Lamb, S. Kenjereš, *Comput. Biol. Med.* **2021**, *133*, 104385.

[14] Y. C. Zhao, P. Vatankhah, T. Goh, R. Michelis, K. Kyanian, Y. Zhang, Z. Li, L. A. Ju, *Sci. Rep.* **2021**, *11*, 1.

[15] G. Troianowski, C. A. Taylor, J. A. Feinstein, I. E. Vignon-Clementel, *J. Biomech. Eng.* **2011**, *133*, 111006.

[16] G. Arbia, C. Corsini, M. Esmaily Moghadam, A. L. Marsden, F. Migliavacca, G. Pennati, T.-Y. Hsia, I. E. Vignon-Clementel, *J. Surg. Res.* **2014**, *186*, 44.

[17] C. Corsini, C. Baker, E. Kung, S. Schievano, G. Arbia, A. Baretta, G. Biglino, F. Migliavacca, G. Dubini, G. Pennati, A. Marsden, I. Vignon-Clementel, A. Taylor, T. Y. Hsia, A. Dorfman, Modeling of Congenital Hearts Alliance (MOCHA) Investigators, *Computer Methods in Biomechanics and Biomedical Engineering* **2014**, *17*, 1572.

[18] L. Guérin, C. Coufort-Saudejaud, A. Liné, C. Frances, *J. Colloid Interface Sci.* **2017**, *491*, 167.

[19] G. Frungieri, M. Vanni, *Powder Technol.* **2021**, *388*, 357.

[20] G. Frungieri, M. U. Bäbler, M. Vanni, *Langmuir* **2020**, *36*, 10739.

[21] A. Saxena, J.-S. Kroll-Rabotin, R. S. Sanders, *J. Colloid Interface Sci.* **2022**, *608*, 355.

[22] M. L. Eggersdorfer, D. Kadau, H. J. Herrmann, S. E. Pratsinis, *J. Colloid Interface Sci.* **2010**, *342*, 261.

[23] V. Becker, E. Schlauch, M. Behr, H. Briesen, *J. Colloid Interface Sci.* **2009**, *339*, 362.

[24] L. Durlofsky, J. F. Brady, G. Bossis, *J. Fluid Mech.* **1987**, *180*, 21.

[25] G. Frungieri, M. Vanni, *Can. J. Chem. Eng.* **2017**, *95*, 1768.

[26] M. Vanni, A. Gastaldi, *Langmuir* **2011**, *27*, 12822.

[27] M. Vanni, *Comput. Phys. Commun.* **2015**, *192*, 70.

[28] Z. Ren, Y. M. Harshe, M. Lattuada, *Langmuir* **2015**, *31*, 5712.

[29] Y. M. Harshe, M. Lattuada, *J. Phys. Chem. B* **2016**, *120*, 7244.

[30] G. Frungieri, G. Boccardo, A. Buffo, D. Marchisio, H. A. Karimi-Varzaneh, M. Vanni, *Can. J. Chem. Eng.* **2020**, *98*, 1880.

[31] R. L. Fournier, *Basic Transport Phenomena in Biomedical Engineering*, Taylor & Francis, Philadelphia, PA **2017**.

[32] D. A. Fedosov, H. Noguchi, G. Gompper, *Biomech. Model. Mechanobiol.* **2014**, *13*, 239.

[33] F. Yilmaz, M. Y. Gundogdu, *Korea-Australia Rheology Journal* **2008**, *20*, 197.

[34] A. Arzani, *J. R. Soc., Interface* **2018**, *15*, 20180486.

[35] A. S. Khader, S. B. Shenoy, R. B. Pai, G. S. Kamath, N. M. Sharif, V. Rao, *World Journal of Modelling and Simulation* **2011**, *7*, 113.

[36] Y. Zhou, C. Lee, J. Wang, *Journal of Healthcare Engineering* **2018**, *2018*, 4312415.

[37] Q. Long, X. Xu, K. Ramnarine, P. Hoskins, *J. Biomech.* **2001**, *34*, 1229.

[38] G. Lorenzini, E. Casalena, *J. Biomech.* **1862**, *2008*, 41.

[39] R. Thouy, R. Jullien, *J. Phys. A: Math. Theor.* **1994**, *27*, 2953.

[40] E. Lintingre, F. Lequeux, L. Talini, N. Tsapis, *Soft Matter* **2016**, *12*, 7435.

[41] A. Osman, L. Goehring, A. Patti, H. Stitt, N. Shokri, *Ind. Eng. Chem. Res.* **2017**, *56*, 10506.

[42] M. Skoge, A. Donev, F. H. Stillinger, S. Torquato, *Phys. Rev. E* **2006**, *74*, 041127.

[43] J. De Bona, A. S. Lanotte, M. Vanni, *J. Fluid Mech.* **2014**, *755*, 365.

[44] K. L. Johnson, K. Kendall, A. Roberts, P. Roy, *Proc. R. Soc. London, Ser. A* **1971**, *324*, 301.

[45] C. Dominik, A. Tielens, *The Astrophysical Journal* **1997**, *480*, 647.

[46] J. Marshall, *J. Comput. Phys.* **2009**, *228*, 1541.